Key Points:
- We show a new combined PET/CT imaging for laboratory core analysis
- The signal-to-noise ratio is an order of magnitude higher for PET compared to CT
- Uncertainty in fluid saturation is a factor of 2 lower for PET

Supporting Information:
- Supporting Information S1
- Movie S1

Correspondence to:
M. A. Fernø,
Martin.Ferno@ift.uib.no

Combined positron emission tomography and computed tomography to visualize and quantify fluid flow in sedimentary rocks

M. A. Fernø[1], J. Gauteplass[1], L. P. Hauge[1], G. E. Abell[2], T. C. H. Adamsen[2,3], and A. Graue[1]

[1]Department of Physics and Technology, University of Bergen, Bergen, Norway, [2]Centre for Nuclear Medicine and PET, Department of Radiology, Haukeland University Hospital, Bergen, Norway, [3]Department of Chemistry, University of Bergen, Bergen, Norway

Abstract Here we show for the first time the combined positron emission tomography (PET) and computed tomography (CT) imaging of flow processes within porous rocks to quantify the development in local fluid saturations. The coupling between local rock structure and displacement fronts is demonstrated in exploratory experiments using this novel approach. We also compare quantification of 3-D temporal and spatial water saturations in two similar CO_2 storage tests in sandstone imaged separately with PET and CT. The applicability of each visualization technique is evaluated for a range of displacement processes, and the favorable implementation of combining PET/CT for laboratory core analysis is discussed. We learn that the signal-to-noise ratio (SNR) is over an order of magnitude higher for PET compared with CT for the studied processes.

1. Introduction

Techniques for in situ visualization are vital tools to study flow within opaque systems like the human body or porous rock samples. One important area where such techniques are frequently used today is the retention of injected carbon dioxide in the subsurface, where mechanisms for secure, long-term storage and high storage capacity must be understood. The injected CO_2 is retained in subsurface under an impermeable layer and trapped in the pore space of sedimentary rock by processes such as fluid dissolution, capillary trapping, and mineral reaction [*Benson and Cole*, 2008]. Noninvasive, nonperturbing methods to obtain information of such processes include X-ray computed tomography (CT), magnetic resonance imaging (MRI), and positron emission tomography (PET). To our knowledge, combined PET/CT has not yet been reported in geophysical research.

This work demonstrates a successful implementation of a new PET/CT imaging approach for laboratory core analysis tested using well-known displacement mechanisms. Flow injection tests in consolidated sediments are visualized to quantify 4-D in situ fluid saturation during water-water displacements and CO_2 injections for storage. We evaluate the performance and applicability of PET/CT in rock samples with differences in size, rock structure, and geometry, and compare results with standard CT. Standard CT imaging makes it possible to distinguish between fluid phases with sufficient density difference in core samples with satisfactory porosity. In low-porosity samples with tight rock matrix and small pore volumes, however, fluids must be doped to ensure satisfactory fluid saturation calculation. For such systems, PET imaging with explicit fluid measurement should be used because PET is independent of changes in fluid properties or rock structure to provide superior image quality. The combined PET/CT imaging is directly compared with standalone CT during identical CO_2 injection tests, and differences in applicability, signal-to-noise ratios (SNR), and uncertainties are discussed.

2. Methods and Materials

Next, a description of PET and CT imaging techniques follow, where the underlying physical phenomena are briefly reviewed. The experimental setup and experimental approach during flow tests and the calculation of spatial fluid saturations for each method are provided.

Table 1. Rock System Dimensions, Storage, and Flow Properties

System Type	Rock Type	Dia (cm)	W (cm)	H (cm)	Angle (°)	Length (cm)	Volume (cm^3)	PV (cm^3)	φ (%)	K (mD)
Standard system	Stevns Klint	3.81			0	10.80	125.0	57.6	46.1	3.4
Large system	Rørdal		5	10	0	13.80	690	304	44	5
Tilted system	Bentheim	5.07			13.1	14.19	287	65.1	22.7	1184
Reference CT system	Bentheim	5.03			0	9.95	198	47.0	23.4	~1100

2.1. X-Ray Computed Tomography (CT)

CT measures the X-ray attenuation through gradual loss in flux intensity through the medium and produces a time-averaged density distribution image of the rock [*Heindel*, 2011]. CT was originally developed for clinical use but is also widely used in geosciences [*Blunt et al.*, 2013; *Cnudde and Boone*, 2013; *Wildenschild and Sheppard*, 2013]. CT imaging relies on sufficient density contrasts which are often not fulfilled in low-porosity media. However, by implementing a high X-ray contrast gas technique, X-ray CT imaging in low-permeability, dual porosity media has recently been achieved [*Vega et al.*, 2014]. Because attenuation depends on both the electron density and the effective atomic number, the CT number will vary with the energy of the rays. At low energy, the attenuation is dominated by photoelectric absorption when an X-ray photon liberates an electron from the inner layers of an atom by giving up its entire energy [*Hsieh*, 2003]. At high photon energy, the dominant attenuation effect is Compton scattering, where the photon is deflected through an angle proportional to the amount of energy lost from the interaction with the recoil electron. Compton scattering is mostly dependent on electron density. Spatial fluid saturation is derived with sufficient fluid density difference.

2.2. Positron Emission Tomography (PET)

Although primarily used as a clinical diagnostic tool, PET has been used to visualize fluids in porous structures including construction materials [*Hoff et al.*, 1996], crystalline rocks [*Degueldre et al.*, 1996], and sediments [*Haugan*, 2000; *Khalili et al.*, 1998; *Maguire et al.*, 1997]. PET visualization of flow fields in porous sandstones was reported by *Ogilvie et al.* [2001], and more recently in other geomaterials [*Dechsiri et al.*, 2005; *Kulenkampff' et al.*, 2008]. PET is based on positron-emitting radionuclides where a positron is emitted from the nucleus accompanied by an electron to balance atomic charge. The positron loses kinetic energy by interactions with the surroundings, and at near-zero momentum, the positron combines with an electron and annihilates. The physics of nucleus decay and annihilation limits the spatial resolution of PET and the achieved resolution depends on the distance to the detectors. A detector array registers the electromagnetic radiation in the form of two 511 keV photons emitted in opposite directions to conserve momentum. The photons are able to penetrate the aluminum confinement vessel holding the rock sample at elevated pressures and are registered only when they are within the coincidence window and the line-of-response (LOR) acceptance angle [*Bailey et al.*, 2005]. Spatial fluid saturation is calculated based on the registered activity of the labeled phase; in this case, the labeled phase is water using the sodium radioisotope ^{22}Na.

2.3. Rock Types, Sample Preparation, and System Descriptions

Three quarried outcrop rock types were used as reservoir analogs: Bentheim sandstones with mainly quartz (95%) [*Ramstad et al.*, 2012] and two outcrop chalks (Stevns Klint and Rørdal) with mainly calcite (>99%) [*Hjuler*, 2007]. PET/CT imaging of fluid flow was evaluated in the following three systems: (1) in the *Standard system*, two cylindrical Stevns Klint cores were horizontally stacked to create a capillary discontinuity in the flow direction, (2) *Tilted system:* upward injection in a 13° tilted cylindrical Bentheim sandstone core plug, and (3) *Large system:* a horizontal rectangular Rørdal sample with a pore volume 5.5 times larger than the *Standard system*. Porosity (φ) was determined by increase in weight after water saturation under vacuum. Absolute permeability (K) was determined using Darcy's law using different flow rates. Rock and system properties are listed in Table 1.

2.4. Fluids and Radioisotopes

Chalk samples were saturated with CaCl$_2$-brine to minimize dissolution ($\mu = 1.09$ mPa·s; $\rho = 1050$ kg/m^3; salts: 5 wt % NaCl and 5 wt % CaCl$_2$·2H$_2$O), whereas sandstone samples were saturated with NaCl-brine ($\mu = 1.07$ mPa·s; $\rho = 1030$ kg/m^3; 5 wt % NaCl). Here we use the positron-emitting sodium isotope ^{22}Na (t$^1/_2$ = 2.6 years) based on previous work [*Ersland et al.*, 2010; *Graue et al.*, 1990; *Lien et al.*, 1988], because (1)

sodium is naturally occurring in the injected brine, (2) the long half-life makes repeated use of tracers possible, and (3) no need to correct for decay because experimental time is ≪half-life. Sodium-22 was shipped to the laboratory in small vials and used as received with 1 mCi (37 MBq) mixed in 1 L brine. NaI (7.5 wt %) was added to the NaCl-brine in CT tests for sufficient density contrast between brine and liquid state CO_2.

2.5. Experimental Setup

Water-saturated core plugs were installed in an aluminum biaxial core holder with a rubber sleeve to apply a radial, confinement pressure to ensure that the injected fluid was transported through the pore space. A rectangular aluminum vessel was used to apply a confinement pressure for the block sample cast in a two-component epoxy resin with aluminum end pieces for fluid injection and distribution. High-pressure injection pumps were used for controlled flow conditions and to maintain confinement and pore pressures. Radioactive brine was stored in steel accumulators and injected with constant volumetric flow rate or constant injection pressure. A Siemens Biograph Truepoint PET-CT scanner was utilized for all tests where the rock samples were placed in the center of the PET/CT bore (diameter 700 mm—axial field of view of 169 mm). The spatial voxel size was for CT 0.156 mm^3 (0.51 × 0.51 × 0.6 mm^3) and for PET 8.49 mm^3 (2.04 × 2.04 × 2.04 mm^3).

2.6. Calculating Spatial Fluid Saturations

CT measures the spatial, average attenuation in each voxel where both rock and fluid phases are present. The acquired attenuation distribution cannot quantify porosity or fluid saturation directly, on an individual voxel basis, and spatial attenuation of the system when the pores are 100% filled with each fluid is needed. With a single fluid present in the pore space, each voxel has a linear combination of attenuation from both the rock and the fluid [*Withjack*, 1988]. The attenuation coefficient for a mix of phases will depend on the attenuation coefficient of the individual components and their saturation [*Akin and Kovscek*, 2003; *Vinegar and Wellington*, 1987]. CO_2 saturation can also be expressed in terms of CT number (Hounsfield units). In the case of water and CO_2:

$$S_{CO_2} = \frac{CT_{wr} - CT_{co_2wr}}{CT_{wr} - CT_{co_2r}}$$ (1)

where CT_{wr} is the CT number for fully water-saturated rock, CT_{co_2r} the CT number for fully CO_2-saturated rock, and CT_{co_2wr} the CT number measured during the experiment. Comparable results between PET and CT measurements were obtained by increasing the CT voxel size from the original 0.156 mm^3 to ∼8.5 mm^3 (PET resolution). This was done by averaging a number of neighboring voxels to arrive at a measured CT number with PET resolution.

PET on the other hand measures the photons emitted from the tracer, while the rock remains undetected. The recorded number of disintegrations may be used to calculate the spatial saturation of the labeled fluid (brine in this work). An assumption is that the radioisotopes remain in the aqueous phase, and tracer adsorption on the pore wall is minimized by preinjection of several pore volumes of regular brine [*Bailey et al.*, 1981; *Graue et al.*, 1990]. Fluid saturations may then be found from the linear relationship between the number of disintegrations and the saturation of the labeled fluid, described as:

$$S_w = \frac{I_{x,y,z}}{A_{x,y,z}}$$ (2) AQ2

where S_w is the saturation of the labeled phase (water) at location (x,y,z), I is the time-averaged radiation intensity at location (x,y,z), and A is the time-averaged intensity value of 100% phase saturation at location (x,y,z). The recorded number of disintegrations is attenuation corrected for spatial density variations within the field of view using the CT scan. Random events are corrected using Delayed Event Subtraction, while scattering is model-based corrected. Only small amounts of tracer are needed to achieve a superior SNR compared with conventional attenuation techniques.

3. Results and Discussion

We now demonstrate the novel combination of PET and CT for miscible water-water displacements in systems with variations in size and geometry. The injected water phase was labeled with [22]Na tracers. In
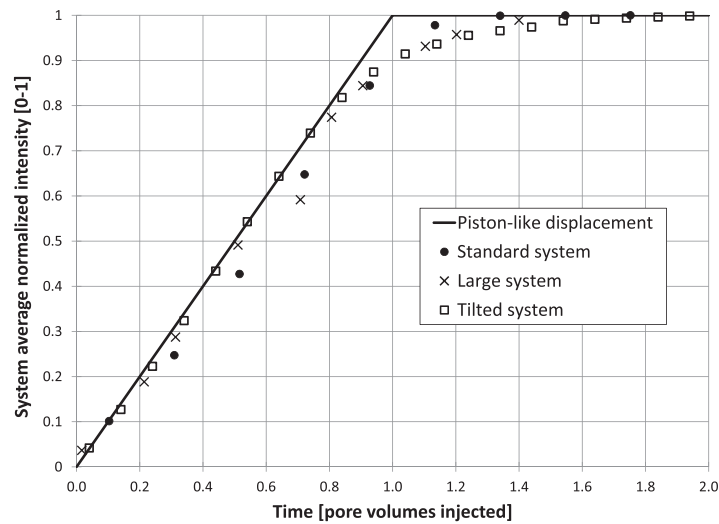
Figure 1. Comparison between the averaged normalized injected water phase saturation during the miscible water-water injections in three systems: solid circles (*Standard System*), crosses (*Large System*), and open squares (*Tilted System*). The experimental data are compared to a pure piston-like displacement (solid, black line).

addition, we compare PET visualization of CO_2 injection with medical CT imaging and discuss differences in applicability and SNR.
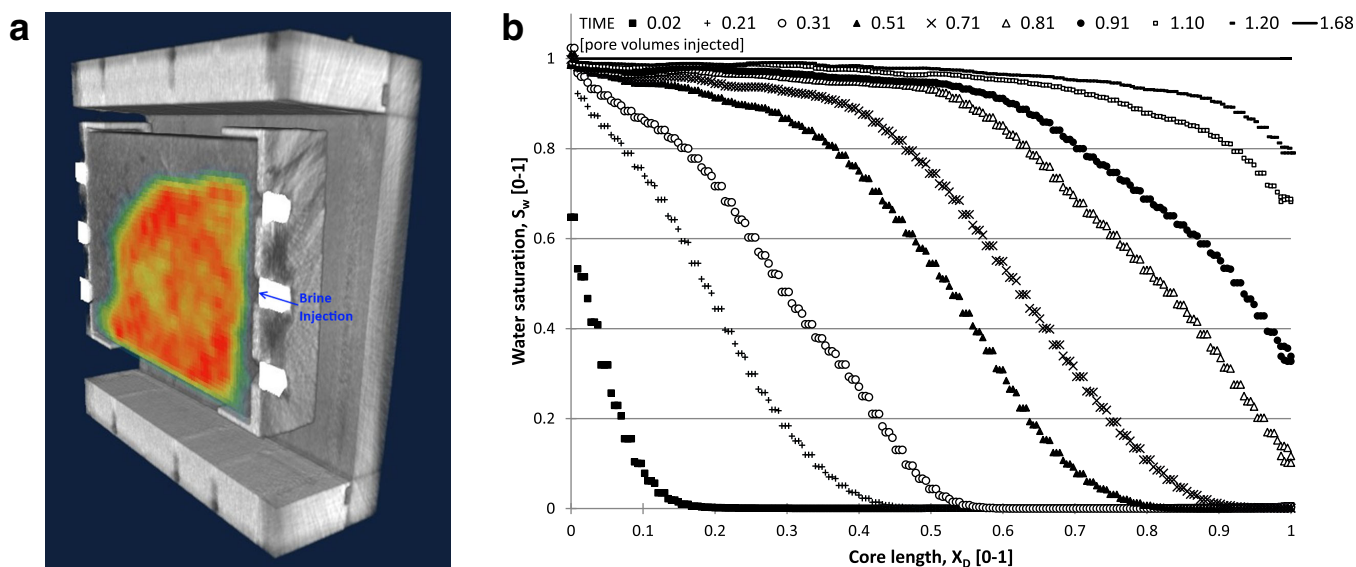
3.1. PET: Miscible Water-Water Displacement

The average water saturation versus pore volumes injected during a fully miscible water-water displacement should, in a perfectly uniform system, be a line with constant slope and breakthrough after 1 pore volume injected (see Figure 1)—this is called a piston-like displacement [*Skjaeveland and Kleppe*, 1992]. Deviation from the piston-like displacement, through development of preferred flow paths such as water fingers, is directly related to the pore structure and the level of uniformity. All three natural porous systems studied here (*Standard, Large*, and *Tilted*) deviate slightly from the piston-like displacement as a result of local heterogeneity, with earlier water breakthrough (t < 1 PV) and slower increase in the average water saturation after breakthrough. Miscible displacement processes can be used to study flow variations related to local heterogeneities. In that regard, simultaneous decoupled structural rock information (CT) and explicit fluid saturation information (PET) provides a robust imaging technique.

In the *Standard system*, a piston-like displacement was initially observed from PET data and the injected water profiles maintained their shape over time. Two cylindrical chalk cores were horizontally stacked to create a capillary discontinuity in the flow direction (see Figure 2). A 3-D CT image intersected with a 2-D PET slice illustrates how the explicit PET signal relates spatially to the CT image (left). Viscous fingers formed when the water reached the discontinuity, but did not develop to establish an unstable front, likely due to system size constraints. In this work, we define the front of a displacement between two phases (miscible or
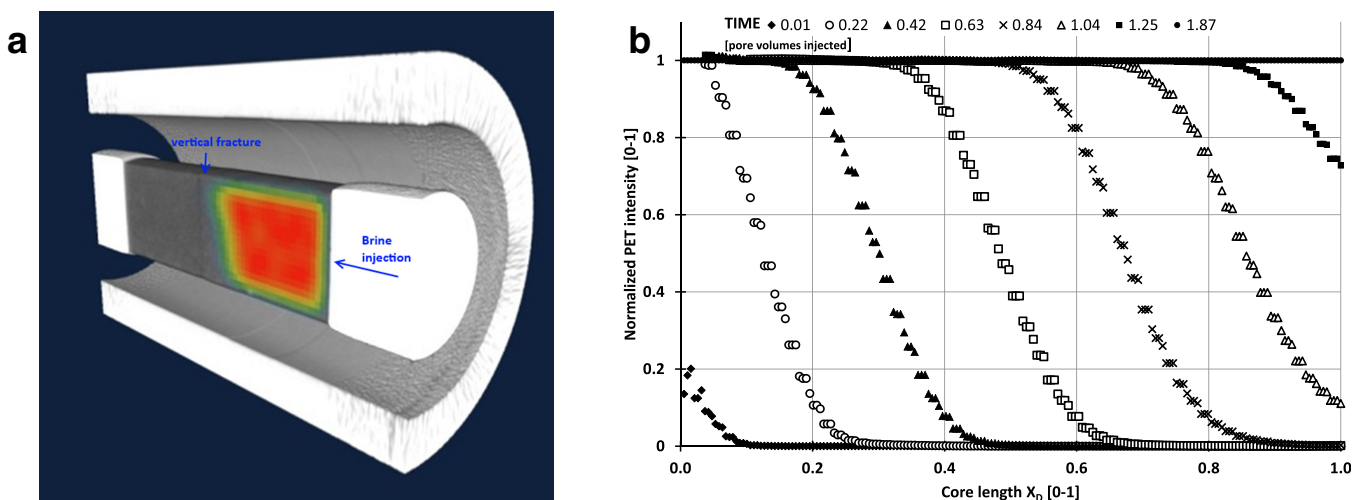
Figure 2. Miscible water-water displacement (Q = 12 cm^3/h, P = ambient, T = 23°C) in *Standard system* (horizontally stacked Stevns Klint core plugs). (left) Combined 3-D CT (gray scale) and 2-D PET data after 0.52 PV injected. Two-dimensional color map shows distribution of ^{22}Na-brine intensity in the system. (right) Quantitative 1-D water saturation profiles calculated from PET measurements. A slightly dispersed front maintains its shape over time.

Figure 3. Miscible water-water displacement ($Q = 30$ cm^3/h, $P =$ ambient, $T = 23°C$) in *Large system* (rectangular Rørdal chalk block). (left) Combined 3-D CT (gray scale) and 2-D PET data after 0.81 PV injected. Two-dimensional color map shows distribution of ^{22}Na-brine intensity in the system. The aluminum end pieces on both sides of the block are easily observed, as well as the three fittings on each side for fluid injection and production. (right) One-dimensional water saturation profiles calculated from PET measurements. The front becomes increasingly disperse over time.

immiscible) as the initial 0–5% saturation increase of the advancing fluid. One-dimensional (1-D) quantitative water saturation profiles (equation (2)) demonstrated a slightly dispersed front advancing through the core with a constant velocity. The effect of size was evaluated using the *Large system:* a horizontal rectangular sample with a pore volume 5.5 times larger than the *Standard system*. Here the injected water entered the block at the bottom and advanced predominantly in the lower parts of the rectangular block (see Figure 3). The front was not smooth, and fingers of the injected water phase were allowed to develop as fewer boundary effects existed here (in contrast to the *Standard system*). The 1-D profile became increasingly dispersed over time as a result of the developing viscous fingers. The injected ^{22}Na-brine front expands from 0.1 to 0.8 of the normalized length in the *Large system* after 50% of the pore volume has been injected, as compared to the *Standard system*, in which the front is confined between 0.35 and 0.6 after 0.5 PV (seen in Figures 2b and 3b, respectively). The normalized water saturation profiles are generated within the area of the block that was completely saturated by injected water at the end of the test.

3.2. Case Study PET Versus CT: CO$_2$ Injection for CO$_2$ Storage

Here we compare combined PET/CT imaging to standard medical CT imaging during liquid CO$_2$ injection to evaluate the CO$_2$ storage potential in saline aquifers. We quantify 4-D water saturations in two separate CO$_2$ injection tests using either PET or CT.

Spatial fluid saturations from PET showed preferred CO$_2$ flow paths along the edges of the slightly tilted Bentheim sandstone core with water remaining in the center (Figure 4). At steady state a CO$_2$ saturation gradient was observed, with $S_{CO_2} = 0.50$ at the inlet ($X_D = 0.01$) and $S_{CO_2} = 0.03$ at the outlet ($X_D = 0.99$). Fluids were not equilibrated prior to injection, adding a dissolution effect near the inlet to the otherwise immiscible displacement [*Berg et al.*, 2013]. The liquid CO$_2$ saturation in the representative area of the core was 0.23 and matches previous reported values at the pore scale [*Chaudhary et al.*, 2013; *Iglauer et al.*, 2011] and at the core scale [*Krevor et al.*, 2012; *Pini et al.*, 2012]. Under identical conditions, liquid CO$_2$ was injected in a horizontal Bentheim core sample and imaged with standard CT (Figure 5). Consistent with the PET experiment, we observed that CO$_2$ mainly displaced water in the outer radius of the cylindrical core plug, resulting in higher water saturation in the center of the core, with an average $S_{CO_2} = 0.25$. It is evident that both techniques are able to image the experimental procedure, providing essential in situ fluid distribution to address the displacement mechanisms during CO$_2$ injection. Next, we focus our discussion on the differences between PET and CT visualization and highlight areas where each method has strengths and compare applicability.
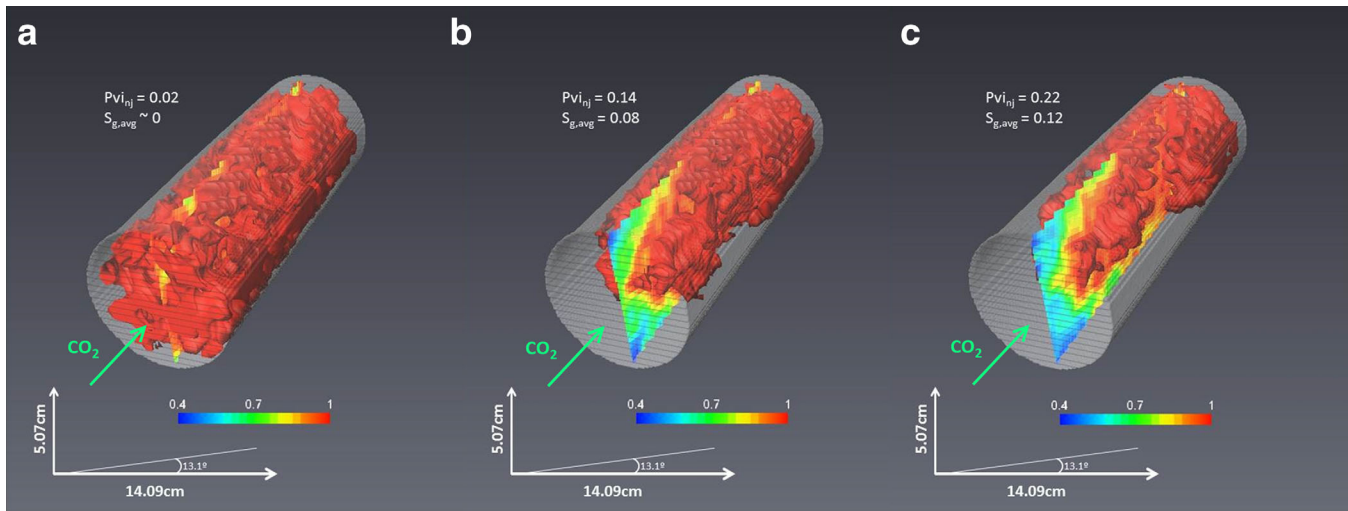
Figure 4. Spatial 3-D water distribution calculated with PET in a tilted (13°) sandstone core plug during liquid CO_2 ($\mu = 0.074$ mPa·s; $\rho = 818$ kg/m^3) injection with a constant volumetric rate (Q = 2.5 cm^3/h—$N_C = 7.6 \cdot \times 10^{-10}$, P = 9 MPa, T = 23°C). As CO_2 migrates upward, CO_2 flow paths form along the edges and water remains in the center. A CO_2 saturation of 0.23 was observed in the middle of the core, but a CO_2 saturation gradient was present at steady state (2.54 pore volumes CO_2 injected). An isosurface (in red) shows distribution of 100% water saturation. Small deviations in pore volume injected and gas saturation is caused by dissolution of CO_2 and compression of injection fluid.

We evaluate the scientific significance of each visualization technique based on the range of processes it can study and the SNR related to these processes. As demonstrated above, both PET and CT are able to visualize injection of CO_2 under the experimental conditions studied using high-quality sandstone core plugs. Considering water-water displacements, PET is more suitable for determining front progression than CT. Calculation of spatial fluid saturations during mixing of similar fluids is challenging for CT because of the relatively low fluid density contrast. PET calculation of fluid saturation relies on the positron emission from the labeled fluid (the injected brine), and is therefore independent on fluid density contrast. Although PET measures fluids explicitly, CT provides a direct measurement of rock structure based on density distribution. Flow and structure data may then be aligned and correlated to study relevant fluid flow mechanisms in
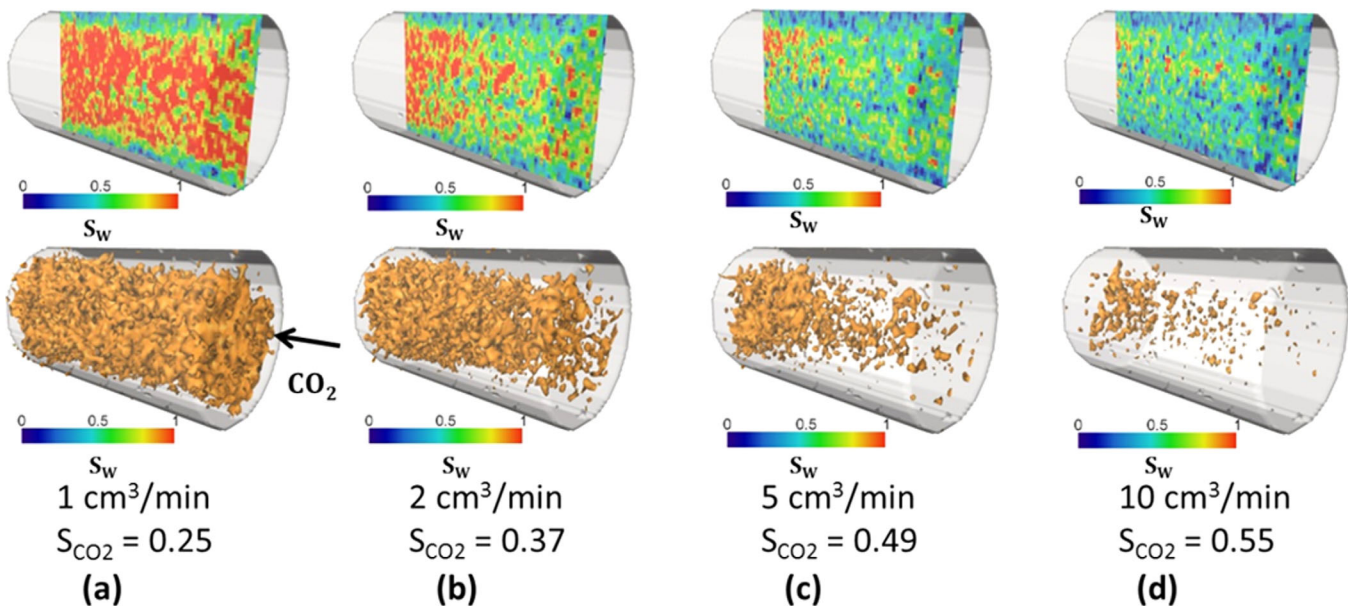
Figure 5. Spatial 3-D water distribution calculated with CT measurements during liquid CO_2 ($\mu = 0.074$ mPa·s; $\rho = 818$ kg/m^3) injection from right to left (indicated by the arrow) using different rates. Approximately 1.3 PV is injected for each rate before a CT scan is acquired ($N_C = 1.7 \times 10^{-8}$, 3.5×10^{-8}, 8.7×10^{-8}, and 1.7×10^{-7}, P = 9 MPa, T = 23°C). (top) Color mapping shows the sagittal water saturation distribution. (bottom) The isosurface shows the distribution of the high water-saturated areas of the core (threshold $S_W > 0.9$). The resolution was reduced to 0.74 mm^3, and a Gaussian mean averaging over 2 pixel radius was applied to reduce the uncertainty in the 3-D results. Images are rendered using Avizo imaging software. Note that the water saturation is higher in the middle of the core and a relatively high saturation remains in the center close to the outlet.

Table 2. Comparison Between PET/CT and Standalone CT to Characterize Fluid Flow in Porous Media

	PET/CT	Standalone CT
General comparison	*Advantages*	*Advantages*
	Tracers can be added to both aqueous and gaseous phases	Three phase capabilities
	Reference scan of tracked fluid only	Higher spatial resolution
	Fluid quantified in all quality rocks	*Limitations/Drawbacks*
	Signal temperature/pressure independent	Reference scans of all fluids present
	Excellent to evaluate front of tracked fluid (Figures 1–3)	Need sufficient density contrast
	Limitations/Drawbacks	Temperature/pressure sensitive
	Restricted PET spatial resolution	Require adequate porosity/fluid volume
	Radioactive fluid handling	System symmetry often required
	Tracer adsorption on rock surface	Cannot determine fluid fronts (S < 5%)
		Temporal resolution cannot be set postprocessing
SNR voxel, S_W calc.	200:1	16:1[a]
SNR voxel, Front	10:1	0.8:1[a]
ΔS_W, 3-D [frac.]	±0.04[b]	±0.08[a]
ΔS_W, 1-D [frac.]	±0.01	±0.02
Instrument Specifics		
Spatial resolution	2.04 × 2.04 × 2.04 mm	0.51 × 0.51 × 0.6 mm
Temporal resolution	30 min[c]	10 s
Photon energy	511 keV	140 keV
Exposure		300 mAs

[a]CT images are scaled to PET resolution for standard deviation measurements.
[b]The uncertainty for PET signal is one standard deviation at a location without saturation change.
[c]Signals are continuously recorded and temporal resolution is set during postprocessing. With increased signal intensity temporal resolutions of 10 s with similar SNR can without difficulty be achieved.

sediments through the two decoupled imaging techniques. Hence, combined PET/CT provides complementary information that exceeds information from each method separately, and can be applied to a larger range of rock types and displacement processes.

When we compare PET and CT SNR for the flow processes studied, we find that PET has more than an order of magnitude better SNR during (1) *fluid calculation in CO_2-brine systems*: 200:1 (PET) compared with 16:1 (CT); (2) *detecting displacement fronts*: 10:1 (PET) compared with 0.8:1 (CT). The PET signal is the registered number of positron emission in ROI (>1000 voxels in rock sample—8.0 cm^3), whereas the CT signal is the Hounsfield difference between reference scans in ROI. The PET noise is the average signal in ROI without tracer present, and CT noise is the standard deviation within a ROI with uniform density. Hence, the SNR for CT imaging is the ratio of Hounsfield unit difference, between a fully water-saturated sample and fully CO_2-saturated sample, to the variation in Hounsfield units observed in an area of stable saturation (the standard deviation). The displacement front is the initial 0–5% saturation increase in an advancing fluid front. With the medical CT scanner used in this work, combined with the definition of the fluid front, we cannot accurately define the fluid front in CO_2-brine system using standalone CT as the noise exceeds the signal. The SNR may be improved for both methods by either increasing the density difference of fluids present (CT), or by increasing the activity of the radioisotope labeling the fluid (PET). The CT signal, as defined above, is also indirectly affected by operating parameter (kV, mA s, and pitch) and reconstructing parameters (including filter used, slice thickness, and reconstructing algorithm), but will not be further discussed here. Salts added to increase brine density will increase the signal range between CT reference scans (obtained at $S_{CO_2} = 1.0$ and at $S_w = 1.0$) and thus improve SNR. Enhanced SNR should, however, be weighed against changes in fluid properties and fluid-rock interactions with excess salt concentrations. Because CT relies on density differences, the approach is also sensitive to variations in experimental conditions that will influence fluid density such as temperature and pressure. In contrast, the positron decay is not sensitive to temperature or pressure [*Emery*, 1972]. In addition, the polychromatic CT X-ray diagram may produce beam hardening artifacts, whereas the monochromatic photon origin excludes beam hardening in PET imaging. The low energy (140 keV) associated with CT results in a combination of photoelectric effect and compton scattering. Positron emission annihilates at a single higher energy (511 keV) and matter interaction is dominated by compton scattering. Using equations (1) and (2), we calculate the uncertainties in the spatial fluid saturations at $S_w = 0.50$ for CT: $\Delta S_w = 0.11$ (per 3-D voxel) and $\Delta S_w = 0.02$ (1-D), and for PET: $\Delta S_w = 0.04$ (per 3-D voxel)

and $\Delta S_W = 0.01$ (1-D). Again, we see that PET provides higher accuracy in fluid saturation for both 3-D visualization and 1-D profiles, see also Table 2. The reported range uncertainties and SNR in Table 2 are not exclusive for CO_2-brine and water-water displacements studied here, but remain valid for other displacements like, e.g., oil-water or other immiscible displacements in porous media.

4. Conclusions

In this technical note, we demonstrate the implementation of a new robust, decoupled PET/CT imaging approach to provide dynamic 3-D fluid saturations in laboratory core analysis. We do not present an exhaustive sensitivity study, but rather demonstrate its applicability in well-known displacement mechanisms and present the following key observations:

1. For the first time, we combine positron emission tomography (PET) and computed tomography (CT) to visualize and spatially align *quantitative* fluid saturations and flow with local rock structure in porous media.
2. Combined PET/CT provides complementary information that exceeds information from each method separately, and can be applied to a larger range of rock types and displacement processes.
3. PET is superior compared with CT to determine front progression during flow injection tests and to calculate spatial fluid saturation in porous sediments. The signal-to-noise ratio (SNR) is more than an order of magnitude higher for PET compared with CT, and uncertainty in local fluid saturation is a factor of 2 lower for PET compared with CT at studied conditions.
4. Based on our findings, we learn that PET imaging has a great potential in low-porosity samples (e.g., shale) because of explicit fluid measurement that provides high image quality and SNR independent of low pore volume and rock structure.

Notation

Abbreviations

CT   computed tomography.
MRI   magnetic resonance imaging.
PET   positron emission tomography.
PV   pore volume.
SNR   signal-to-noise ratio.
ROI   region of interest.

Nomenclature

$A_{x,y,z}$ time-averaged intensity value of 100% phase saturation at location (x,y,z).
CT_{wr} CT number for fully water-saturated rock.
CT_{co_2r} CT number for fully CO_2-saturated rock.
CT_{co_2wr} CT number measured during the experiment.
$I_{x,y,z}$ time-averaged radiation intensity at location (x,y,z).
K absolute permeability.
N_c capillary number.
P pressure.
Q injection rate.
S_{CO_2} liquid CO_2 saturation.
S_w water saturation.
S_{wi} initial water saturation.
ΔS_W uncertainty in water saturation.
t time.
T temperature.
X_D normalized length.
φ porosity.

References

Akin, S., and A. R. Kovscek (2003), Computed tomography in petroleum engineering research, *Geol. Soc. Spec. Publ.*, *215*(1), 23–38.

Bailey, D. L., D. W. Townsend, P. E. Valk, and M. N. Maisey (Eds.) (2005), *Positron Emission Tomography*, Springer, London, U. K.

Bailey, N. A., P. R. Rowland, and D. P. Robinson (1981), Nuclear measurements of fluid saturation in EOR flood experiments, paper presented at European Symposium on Enhanced Oil Recovery, UK Department of Energy, Bournemouth, U. K., 21–23 Sept.

Benson, S. M., and D. R. Cole (2008), CO_2 sequestration in deep sedimentary formations, *Elements*, *4*(5), 325–331.

Berg, S., S. Oedai, and H. Ott (2013), Displacement and mass transfer between saturated and unsaturated CO_2–brine systems in sandstone, *Int. J. Greenhouse Gas Control*, *12*, 478–492, doi:10.1016/j.ijggc.2011.04.005.

Blunt, M. J., B. Bijeljic, H. Dong, O. Gharbi, S. Iglauer, P. Mostaghimi, A. Paluszny, and C. Pentland (2013), Pore-scale imaging and modelling, *Adv. Water Resour.*, *51*, 197–216, doi:10.1016/j.advwatres.2012.03.003.

Chaudhary, K., M. Bayani Cardenas, W. W. Wolfe, J. A. Maisano, R. A. Ketcham, and P. C. Bennett (2013), Pore-scale trapping of supercritical CO_2 and the role of grain wettability and shape, *Geophys. Res. Lett.*, *40*, 3878–3882, doi:10.1002/grl.50658.

Cnudde, V., and M. N. Boone (2013), High-resolution X-ray computed tomography in geosciences: A review of the current technology and applications, *Earth Sci. Rev.*, *123*, 1–17, doi:10.1016/j.earscirev.2013.04.003.

Dechsiri, C., A. Ghione, F. van de Wiel, H. G. Dehling, A. M. J. Paans, and A. C. Hoffmann (2005), Positron emission tomography applied to fluidization engineering, *Can. J. Chem. Eng.*, *83*(1), 88–96.

Degueldre, C., H. Pleinert, P. Maguire, E. Lehman, J. Missimer, J. Hammer, K. Leenders, H. Bock, and D. Townsend (1996), Porosity and pathway determination in crystalline rock by positron emission tomography and neutron radiography, *Earth Planet. Sci. Lett.*, *140*(1–4), 213–225, doi:10.1016/0012-821x(96)00043-X.

Emery, G. T. (1972), Perturbation of nuclear decay rates, *Annu. Rev. Nuclear Sci.*, *22*(1), 165–202, doi:10.1146/annurev.ns.22.120172.001121.

Ersland, G., M. A. Fernø, A. Graue, B. A. Baldwin, and J. Stevens (2010), Complementary imaging of oil recovery mechanisms in fractured reservoirs, *Chem. Eng. J.*, *158*(1), 32–38.

Graue, A., K. Kolltveit, J. R. Lien, and A. Skauge (1990), Imaging fluid saturation development in long-core flood displacements, *SPE Form. Eval.*, *5*(4), 406–412.

Haugan, A. (2000), A low-cost PET system for use in flow experiments of porous media, paper presented at SPE Annual Technical Conference and Exhibition, Soc. of Pet. Eng., Dallas, Tex., 1–4 Oct.

Heindel, T. J. (2011), A review of X-ray flow visualization with applications to multiphase flows, *J. Fluid Eng.*, *133*(7), 074001, doi:10.1115/1.4004367.

Hjuler, M. L. (2007), *Diagenesis of Upper Cretaceous Onshore and Offshore Chalk From the North Sea Area*, Tech. Univ. of Den., Copenhagen.

Hoff, W. D., M. A. Wilson, D. M. Benton, M. R. Hawkesworth, D. J. Parker, and P. Fowles (1996), The use of positron emission tomography to monitor unsaturated water flow within porous construction materials, *J. Mater. Sci. Lett.*, *15*(13), 1101–1104, doi:10.1007/BF00539949.

Hsieh, J. (2003), *Computed Tomography: Principles, Design, Artifacts, and Recent Advances*, SPIE Press, Wash.

Iglauer, S., A. Paluszny, C. H. Pentland, and M. J. Blunt (2011), Residual CO_2 imaged with X-ray micro-tomography, *Geophys. Res. Lett.*, *38*, L21403, doi:10.1029/2011GL049680.

Khalili, A., A. J. Basu, and U. Pietrzyk (1998), Flow visualization in porous media via Positron Emission Tomography, *Phys. Fluids*, *10*(4), 1031–1033, doi:10.1063/1.869627.

Krevor, S. C. M., R. Pini, L. Zuo, and S. M. Benson (2012), Relative permeability and trapping of CO_2 and water in sandstone rocks at reservoir conditions, *Water Resour. Res.*, *48*, W02532, doi:10.1029/2011WR010859.

Kulenkampff, J., M. Gruundig, M. Richter, and F. Enzmann (2008), Evaluation of positron-emission-tomography for visualisation of migration processes in geomaterials, *Phys. Chem. Earth*, *33*(14–16), 937–942, doi:10.1016/j.pce.2008.05.005.

Lien, J. R., A. Graue, and K. Kolltveit (1988), A nuclear imaging technique for studying multiphase flow in a porous medium at oil reservoir conditions, *Nucl. Instrum. Methods Phys. Res.*, *271*, 693–700.

Maguire, R. P., J. H. Missimer, F. Emert, D. W. Townsend, H. Dollinger, and K. L. Leenders (1997), Positron emission tomography of large rock samples using a multiring PET instrument, *IEEE Trans. Nucl. Sci.*, *44*(1), 26–30, doi:10.1109/23.554819.

Ogilvie, S. R., J. M. Orribo, and P. W. J. Glover (2001), The influence of deformation bands upon fluid flow using profile permeametry and positron emission tomography, *Geophys. Res. Lett.*, *28*(1), 61–64, doi:10.1029/2000GL008507.

Pini, R., S. C. M. Krevor, and S. M. Benson (2012), Capillary pressure and heterogeneity for the CO2/water system in sandstone rocks at reservoir conditions, *Adv. Water Resour.*, *38*, 48–59, doi:10.1016/j.advwatres.2011.12.007.

Ramstad, T., N. Idowu, C. Nardi, and P.-E. Øren (2012), Relative permeability calculations from two-phase flow simulations directly on digital images of porous rocks, *Transp. Porous Media*, *94*(2), 487–504, doi:10.1007/s11242-011-9877-8.

Skjaeveland, S. M., and J. Kleppe (Eds.) (1992), *SPOR Monograph—Recent Advances in Improved Oil Recovery Methods for North Sea Sandstone Reservoirs*, Norw. Pet. Dir., Stavanger, Norway.

Vega, B., A. Dutta, and A. Kovscek (2014), CT imaging of low-permeability, dual-porosity systems using high X-ray contrast gas, *Transp. Porous Media*, *101*(1), 81–97, doi:10.1007/s11242-013-0232-0.

Vinegar, H. J., and S. L. Wellington (1987), Tomographic imaging of three-phase flow experiments, *Rev. Sci. Instrum.*, *58*(1), 96–107, doi:10.1063/1.1139522.

Wildenschild, D., and A. P. Sheppard (2013), X-ray imaging and analysis techniques for quantifying pore-scale structure and processes in subsurface porous medium systems, *Adv. Water Resour.*, *51*, 217–246, doi:10.1016/j.advwatres.2012.07.018.

Withjack, E. M. (1988), Computed tomography for rock-property determination and fluid-flow visualization, *SPE Formation Evaluation*, *3*(4), 696–704, doi:10.2118/16951-PA.